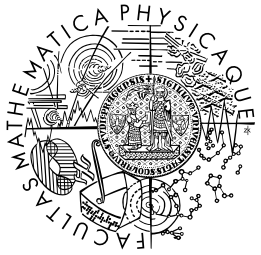

FACULTY
OF MATHEMATICS
AND PHYSICS
Charles University

BACHELOR THESIS

Martin Divíšek

Time calibration of the ATLAS Tile Calorimeter

Institute of Particle and Nuclear Physics

Supervisor of the bachelor thesis: doc. RNDr. Tomáš Davídek, Ph.D.
Study programme: Physics (B1701)
Study branch: FOF (1701R026)

Prague 2022

I declare that I carried out this bachelor thesis independently, and only with the cited sources, literature and other professional sources. It has not been used to obtain another or the same degree.

I understand that my work relates to the rights and obligations under the Act No. 121/2000 Sb., the Copyright Act, as amended, in particular the fact that the Charles University has the right to conclude a license agreement on the use of this work as a school work pursuant to Section 60 subsection 1 of the Copyright Act.

In ..... date ....

Author's signature

Title: Time calibration of the ATLAS Tile Calorimeter

Author: Martin Divíšek

Institute: Institute of Particle and Nuclear Physics

Supervisor: doc. RNDr. Tomáš Davídek, Ph.D., Institute of Particle and Nuclear Physics

Abstract: Following the end of the maintenance period for the ATLAS detector in LHC, CERN, a series of calibrations have to be performed to ensure the quality of measured data. This thesis details the work done on time calibrations of the Tile Hadronic Calorimeter. The Tile Calorimeter uses multiple time calibration methods; these include calibration via laser (a precise light input sent to the detector's photomultipliers), and splash events analysis (measuring the overall response to high-energy particles traversing the length of the calorimeter). Several available sets of laser and splash data were analysed to determine necessary adjustments to the internal electronics and appropriate software going forward. As of April 2022, we have been able to calibrate roughly two thirds of the calorimeter, and will continue calibration once we can acquire additional data.

Keywords: ATLAS experiment hadronic Tile Calorimeter data analysis time calibration

Contents

Introduction **1**

1 Tile Calorimeter **3**
1.1 Calorimetry 3
1.2 TileCal 3
1.3 Calibration Methods 5
1.4 Time Calibration 6
1.4.1 Time Calibration Using Laser Events 6
1.4.2 Time Calibration Using Splash Events 7

2 Time Calibration in 2021/22 **11**
2.1 Laser Events Calibration 11
2.1.1 Initial Analysis 11
2.1.2 In-Gap/Standalone Comparison 11
2.2 Splash Events Calibration 13
2.2.1 Analysis of October 2021 Runs 13

Conclusion **21**

Bibliography **23**

Introduction

Since its completion in 2008, the Large Hadron Collider at CERN remains the world's most powerful particle accelerator to date, as well as an instrumental piece of technology for the purposes of studying the behaviour of particles in high-energy collisions. The sheer scale of the accelerator enables particles to collide at TeV orders of energy magnitude; in 2010, the first collisions made were achieved at an energy of roughly 3.5 TeV per beam, eventually increasing to 6.5 TeV per beam in 2015. As of this time, the collider is undergoing further extensive upgrades aiming to further increase the beam energy as well as overall luminosity.

As each beam orbits inside one of the two 27-kilometre ring of high-vacuum tubes placed in strong magnetic fields responsible for maintaining their trajectory, they can be made to collide in one of the four highly advanced particle detectors: ATLAS, CMS, ALICE, and LHCb, each with their own particular structure and purpose. Of these four, ATLAS is the largest; serving as one of the two general-purpose particle detectors, it was (and still is) instrumental in the experimental examination of the Standard Model and its possible extensions, as well as the study of potential dark matter components. Along with CMS, it was also one of the two experiments that had confirmed the observation of the elusive Higgs boson in 2012.

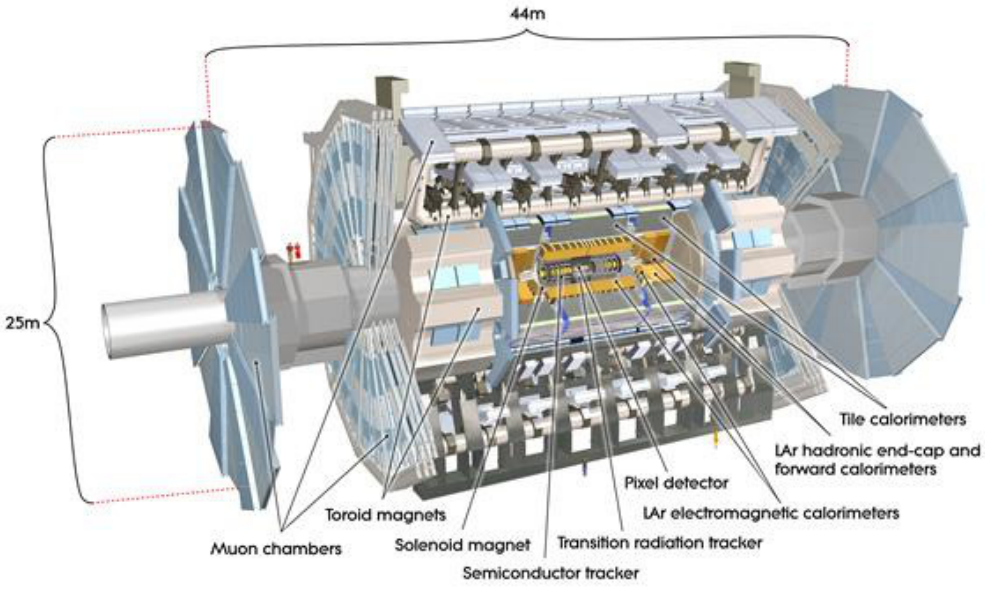

Figure 1: The subsections of the ATLAS Detector [1].

The ATLAS [1] detector itself is comprised of four major subsections: moving from the collision point outwards, these are the Inner Detector, the LAr (Liquid Argon) electromagnetic calorimeters, the Tile hadronic calorimeters, and finally the Muon chambers. These are arranged in layers so that a particle created in the beam collision has to travel through all four in order; each detector then tracks (or doesn't) the trajectory of each particle as it moves through. Measuring the particles' behaviour in strong magnetic fields present in sections of the detector

allows for precise identification of their momentum, charge, and even point of origin, making it possible to reverse-engineer the short-lived primary products of the collision itself.

1. Tile Calorimeter

1.1 Calorimetry

Hadrons, usually further divided into baryons and mesons according to their spin (which further influences their overall quantum behaviour), are all subject to the strong interaction. The principle behind the detector is simple: the incoming particle enters an absorbent layer of high-density material where it interacts with the nuclei, eventually forming a particle shower. The energy of the shower is dependent on the primary particle's energy and observing the shower gives us information about the particle itself.

The particle shower can be further subdivided into two components: the electromagnetic and the hadronic. The two main constituents of the first are electrons and photons; as electrons decelerate in the material, the Bremsstrahlung effect causes them to emit photons, and photons of sufficiently high energy can form e^+e^- pairs. These processes repeat as long as the newly-formed particles have enough energy; eventually, due to other effects that do not create secondary particles (e.g. Compton scattering for photons, non-radiative effects for electrons), the constituents of the electromagnetic shower come to a stop within the detector, having fully deposited their energy.

The hadronic component of the shower is the result of the primary particle's strong interaction in the material. A passing hadron creates a number of secondary hadrons (primarily pions). Due to $\pi^0 \to \gamma\gamma$ decay, an electromagnetic component then forms in the shower ($\gamma \to e^+e^-$ as above); in comparison, primary particles that do not interact strongly cannot create a hadronic component. The hadronic component is also subject to processes that make the full measurement of the hadronic component's energy impossible: nuclear fission, creation of undetectable neutrinos, etc.[1] The response of the detector in regards to the energy of the original particle is therefore nonlinear. These losses can be partially compensated for using appropriate designs and materials [2].

After passing through the absorption layer, the shower enters the active layer. Here, it leaves some kind of measurable signal, usually through scintillation, ionization of the active layer, or Cherenkov radiation. This signal is then gathered, converted into an electric current and processed into data; the particles then enter the next absorption layer, and the process repeats.

1.2 TileCal

The Tile Calorimeter (TileCal) [4] is one of the hadronic detectors responsible for measuring the energy of hadrons passing through the ATLAS detector. The detector is composed of three barrel calorimeters; the central, long barrel (further split into two halves) and two extended barrels at each side of the long barrel. The passive layers are comprised of steel, while the active layer is represented by 3 mm thick tiles of plastic scintillator (hence Tile Calorimeter). These are arranged in a repeating chessboard pattern to provide the best energy resolution

[1] The energy lost in these processes is called invisible energy.

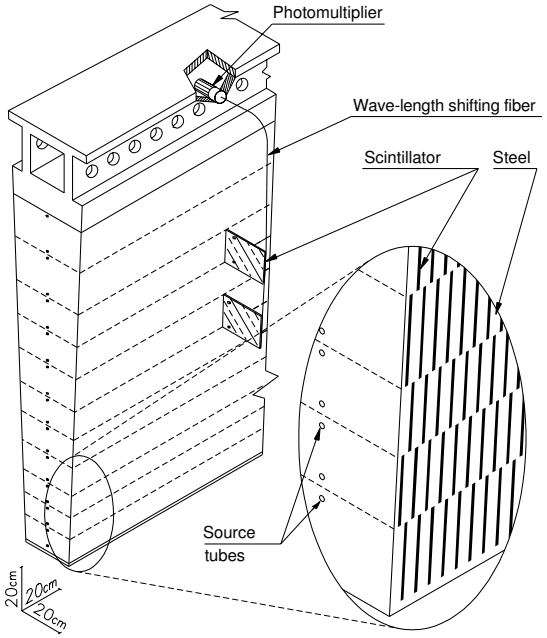

Figure 1.1: Layer arrangement in a TileCal module. Optic fibres placed on each side of every cell collect the scintillated photons and transmit the signal into the appropriate PMT [3].

possible. Each of the three barrels is comprised of 64 individual modules in the azimuthal plane (see Fig. 1.1).

The module itself is segmented into radially aligned readout cells based on the projective geometry of the collision (see Fig. 1.2). These contain the tiles from which the scintillated light is collected via optic fibres, shifted in wavelength, and sent to one of the two photomultipliers, each corresponding to one side of the cell. The PMTs then convert the light into an electric current, which is processed by the detector's front-end electronics.

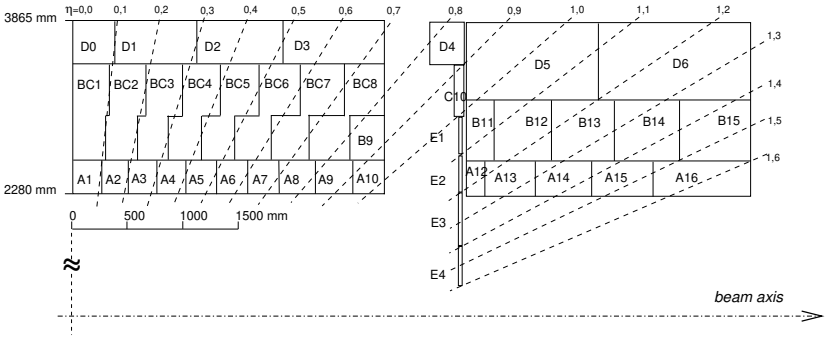

Figure 1.2: Cell segmentation for long and extended barrel [5].

The first such piece of hardware is a 3-in-1 card that is responsible for reading and shaping the initial pulse, then dividing it into two separate branches known as the High (typically 0 GeV-12 GeV) and Low (0 GeV-800 GeV) Gain; the High Gain signal is amplified in a 64:1 ratio. This is to account for the wide energy range of detected particles and serves as a means of separating the comparatively smaller signal from specific particles (muons) from the background noise, while allowing us to measure high energies.

The signal then is processed by a 10-bit analogue-to-digital converter (ADC) unit in each specific gain; the pulse is sampled and digitised every 25 ns and stored in the ADC's pipeline memory. Once the selection algorithm known as the first level trigger determines the event is worth storing, the data in appropriate gain are sent to the read-out driver (ROD) located off-detector.

The energy deposited by the particle in the detector is proportional to the collected charge. Normally, we would have to integrate the signal current over time, but the PMT signal is shaped to have constant width (FWHM of 50 ns). Integration of the signal is not needed; we only have to determine the amplitude. Using the Optimal Filtering algorithm, the amplitude and phase of the signal peak are reconstructed (see Fig. 1.3). When there is no pile-up[2] this process is basically equivalent to regular fitting. After the readout is complete, the ROD forwards the data to the high-level trigger. Here, the data is filtered again, and then sent to external storage.

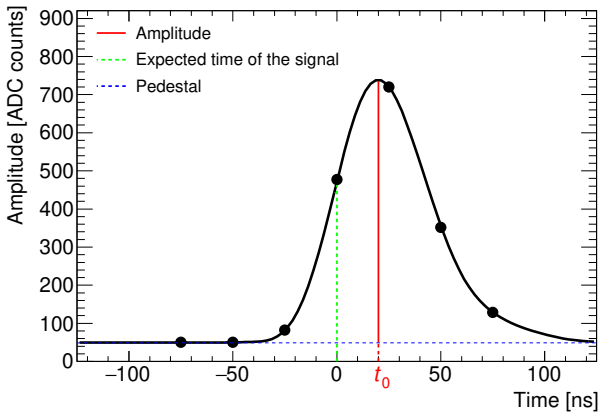

Figure 1.3: OF reconstruction. The shaped analog pulse is represented by seven time samples; the phase t_0 is defined as the offset of the peak position with respect to the central sample.

1.3 Calibration Methods

Proper calibration is key to the precise calorimeter measurement. To this end, TileCal has been equipped with several calibration systems that ensure the quality of its performance. The total energy on the electromagnetic scale for each channel E can be expressed as [3]

$$E = A \cdot C_{\mathrm{ADC\to pC}} \cdot C_{\mathrm{las}} \cdot C_{\mathrm{Cs}} \cdot C_{\mathrm{pC\to GeV}}. \tag{1.1}$$

Here A stands for the amplitude reconstructed in the ADC unit, and the other terms represent individual calibration constants. In order, these are:

- $C_{\mathrm{ADC\to pC}}$ — the conversion factor between the amplitude value reconstructed by the ADC units and the incoming electrical charge from the PMTs. De-

[2]Pile-up occurs when multiple particles collide in the detector in a short time window, and deposit their interaction products into the detector.

termined by the Charge Injection System (CIS) that delivers a well-defined electrical charge into the readout electronics.

- C_{las} — factor determining the relative response of each channel with respect to a known reference. Laser calibration is done via direct illumination of the PMTs by a short laser light pulse, making it possible to measure the individual PMT response and adjust for any possible non-linearities.

- C_{Cs} — calibration constant obtained by measuring the response of the whole optics chain and its associated electronics. A radioactive source (^{137}Cs) is placed inside a special capsule and sent through special tubes passing through all scintillation tiles. This allows for measurement of overall scintillator response shift during data collection, caused by over-time irradiation of the active scintillating tiles and subsequent regeneration during technical breaks. The ^{137}Cs calibration ensures cell response uniformity and is also responsible for the proper definition of absolute energy scale against a known reference.

- $C_{\text{pC}\to\text{GeV}}$ — calibration constant representing the electromagnetic (EM) scale of the detector. Measured during specialized beam tests where selected modules were exposed to secondary particle beams. The mean value of the conversion rate was computed from response to electrons primarily in A-cells, and the EM scale was then further propagated into other rows using ^{137}Cs calibration [2].

1.4 Time Calibration

For the OF algorithm to work properly, the peak of the pulse should be aligned to the middle of the 'readout window'. The phase dependency of the weights used in reconstructing the pulse means that the RMS of the energy amplitude increases considerably as real phase deviates away from zero (see Fig. 1.4).

The timing of the pulse can be adjusted in several ways. The detector itself is equipped with a series of digitizers; electronic units responsible for processing the signal from the PMTs, doing so for groups of six channels at a time. Each digitizer can have its phase adjusted to account for travel time from the detector's initial collision point as well as for delays related to the readout system. Albeit helpful, the grouping of individual channels under a single digitizer cannot account for residual offsets that must be handled during the signal reconstruction. For each event, we define the reconstructed channel time as

$$t_{\text{chan}} = t_0 – t_{\text{const}}. \tag{1.2}$$

t_0 denotes the time phase value (see Fig. 1.3). When the t_{const} values are properly determined, the left side of the equation is equal to zero on average.

1.4.1 Time Calibration Using Laser Events

The laser time calibration utilizes data from laser runs in order to determine the value of the time constants described above. Its primary use is to monitor relative

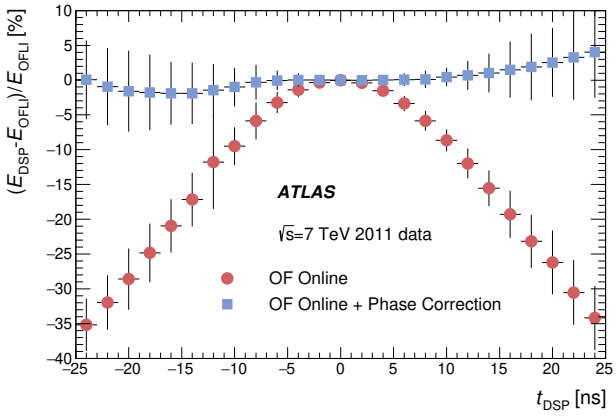

Figure 1.4: Energy reconstructed by the OF algorithm as a function of the real phase. The red points show values when assuming phase equal to zero and follow a quadratic dependence of the energy on the phase. The blue points show values corrected for the real phase. It's clear that for both cases, the error of each point is dependent on distance from phase equal zero [6].

changes in regards to a known default state (after successful time calibration). The individual laser pulses are not synchronised with the internal LHC clock, and must travel from the laser source to the PMTs through fibres of potentially different length. This means the pulse will be arriving at a non-zero time provided that the channel is perfectly optimized for the acquisition of real physics data. Therefore, a separate series of constants must be used:

$$t_{\text{chan}}^{\text{las}} = t_0 - t_{\text{const}}^{\text{las}} - t_{\text{ref}}. \tag{1.3}$$

Here, t_{ref} signifies the reference time (usually taken as the mean of t_0 values across the partition), a correction made to mitigate the offset caused by the laser desync with the LHC clock. Due to its issues, the laser time calibration is primarily used for monitoring; only when the entire detector undergoes extensive hardware changes (such as in advance preparation for the new Run 3 scheduled to start in 2022) is this method also used for preliminary calibrations of each individual channel. Laser data is typically collected in one of the two ways:

- In-gap — the laser pulse is emitted 'in gaps' between individual beam collisions as part of routine physics data collection; the corresponding time window is roughly 5.6 µs long.
- Standalone — the laser data is gathered during a downtime period for the entire detector, typically once per day.

1.4.2 Time Calibration Using Splash Events

Splash events are created by sending an accelerated proton beam into a collimator placed roughly 150 m away from the main interaction point. The beam interacts with the collimator and produces a large amount of secondary particles that traverse the entire detector from one of its two ends to the other on a trajectory

parallel to the z-axis; because of its positioning and geometry, by the time the 'splash' has reached TileCal, most of its constituents have been absorbed, leaving mostly high-energy muons. If we want to properly set the time constants, we must make multiple corrections to account for the point of entry of the 'splash' particle and the differences in travel time to the PMT itself. The splash event reconstructed channel time can be written as

$$t_{\text{splash}} = t_{\text{splash,TOF}} + t_{\text{WLS}} - t_{\text{const}}. \tag{1.4}$$

Here, $t_{\text{splash,TOF}}$ is the Time of Flight of the particle to the corresponding cell, and t_{WLS} is the time of signal propagation from said cell into its PMT, as determined by its specific fibre length. The first of the two can be expressed as

$$t_{\text{splash,TOF}} = T_0 \pm \frac{z_{\text{cell}}}{c}, \tag{1.5}$$

where T_0 represents the reference time taken as the mean reconstructed time from all A±1 and BC±1 cells in the Long Barrel, and z_{cell} denotes the cell centre's z coordinate along the beam axis. Since the splash beam particles possess very high momentum, we assume they travel at the speed of light. The ± sign accounts for the direction of the beam itself. However, the entire detector must be calibrated in regards to particles entering it from the primary interaction point; therefore, further corrections are necessary. We write

$$t_{\text{coll}} = t_{\text{IP,TOF}} + t_{\text{WLS}} - t_{\text{const}}. \tag{1.6}$$

This equation is analogue to (1.2); in other words, the reconstructed time for a particle arriving from a collision at the interaction point is equal to its time of flight needed to reach the cell plus t_{WLS} minus t_{const}. Once more assuming the speed of light, we can substitute $t_{\text{IP,TOF}}$ and rearrange the initial equation as [7]

$$t_{\text{const,new}} = \langle t_{\text{splash}} - T_0 \rangle \pm \frac{z_{\text{cell}}}{c} + \frac{\sqrt{x^2 + y^2 + z^2}}{c} + t_{\text{const}}. \tag{1.7}$$

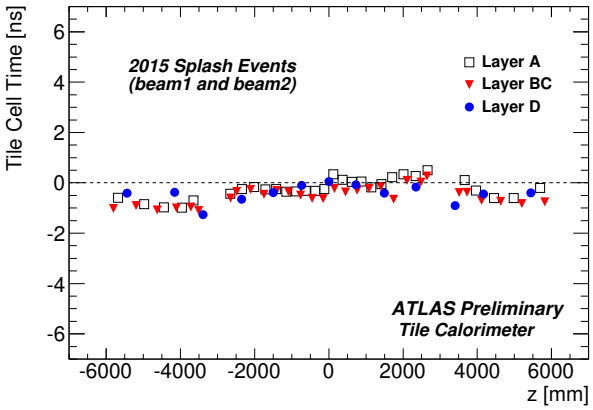

Figure 1.5: ϕ-average reconstructed time from 2015. When the detector is properly calibrated, the application of corrections described above yields a flat distribution centered at zero. The x-axis represents the z-coordinate of the cell centres for each channel, with $z = 0$ in the middle [7].

2. Time Calibration in 2021/22

2.1 Laser Events Calibration

2.1.1 Initial Analysis

Our work was motivated by the upcoming end of the so-called Long Shutdown 2 (LS2) maintenance period (in effect since 2019). During this time, TileCal had undergone several modifications that could, in theory, offset the time calibration of the detector. Among other things, several digitizers had been replaced and the electronics related to the calibration triggers had been modified. In the initial stages of our calibration, we hoped to use in-gap laser data. However, the latest runs available to us at the time were from June 2021 and outdated with respect to the extensive modifications made to TileCal over the summer. Therefore, we had decided to try 'transferring' the constants from 2018 using standalone data.

First, we had examined relative differences between data from November 2018 and June 2021 for each individual type of laser calibration. If correlated, they would allow us to determine the initial values of the constants by evaluating the absolute shift between November 2018 and June 2021 in standalone runs.

To ensure the goodness of the calibration, several cuts were introduced to remove problematic channels. In several channels, the reconstructed laser times did not follow the expected gaussian distribution (usually due to electronics faults, such as stuckbit[1]). These channels cannot yield accurate data, and were removed from the statistic. Figures in 2.1 show the differences between the histogram of a healthy channel and an unhealthy one.

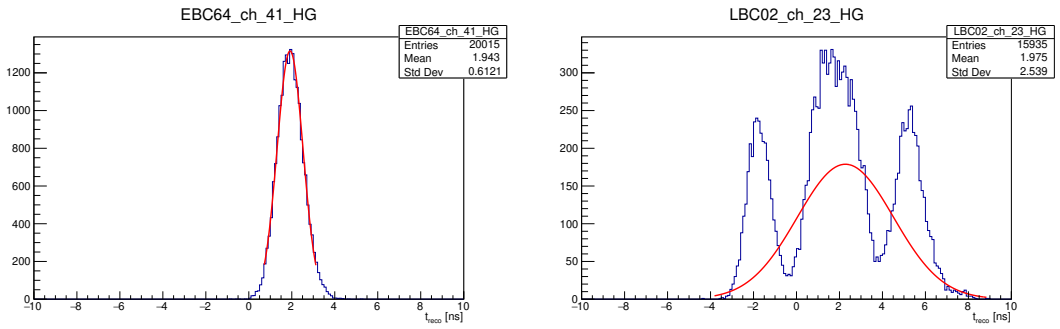

Figure 2.1: Two example histograms of reconstructed times from run 364567 (November 2018 Standalone). The left histogram belongs to a healthy channel, with a clearly gaussian distribution; the histogram on the right suffers from stuckbit.

2.1.2 In-Gap/Standalone Comparison

It was crucial to ensure that the method outlined in the previous subsection would yield accurate results. The individual timing for in-gap and standalone

[1] A stuckbit occurs when one of the 10 bits in the corresponding ADC unit gets 'stuck' on either value, making it impossible to measure the signal accurately.

data is different; it was possible that the relative differences between standalone and in-gap over time would not be correlated well enough to extrapolate in-gap behaviour with sufficient accuracy. Therefore, we tested our hypothesis on the relative shifts in reconstructed time between standalone and in-gap data in the November 2018 to June 2021 period (see Fig. 2.2).

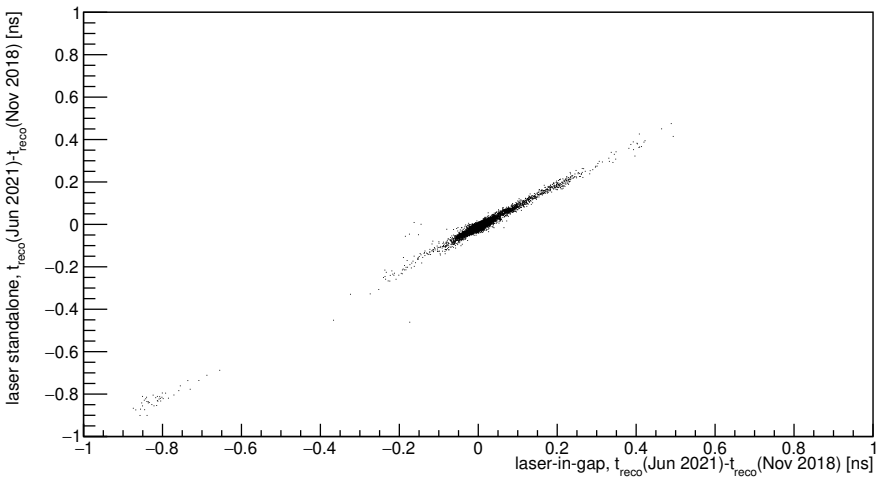

Figure 2.2: A scatter plot of relative shifts in standalone and laser-in-gap reconstructed times between Nov 2018 and Jun 2021. The graph contains roughly 7600 out of 7700 possible channels with the rest being attributed to issues with individual runs.

In the vast majority of cases, the relative shifts in standalone data were indeed highly correlated to the relative shifts in in-gap; over 99 % of the points in Fig. 2.2 deviate from the $y = x$ line by less than 0.1 ns. These results encouraged us to follow through with our method. However, while the relative differences in reconstructed times between both types of laser data are closely tied, the absolute timing is different for each type. To avoid issues with the laser de-sync with the LHC clock, we monitor the mean value of

$$t_{\text{reco}} = tFit - t_{\text{ref}} - t_{\text{const}}^{\text{las}}, \tag{2.1}$$

where t_{reco} describes the reconstructed time to be used when determining the constants, $tFit$ is the phase given by the OF algorithm, and t_{ref} is the same as in equation (1.3), taken over all healthy channels in the given partition for each individual event. Finally, it is worth noting that $t_{\text{const}}^{\text{las}} = 0$ for all standalone runs. The values of t_{ref} are generally different for in-gap and standalone data[2] and can generally change for each data type after significant hardware adjustments. Therefore, an analysis of the individual t_{ref} changes per partition was made for data between standalone 2018 and standalone 2021 runs (see Fig. 2.3).

For the purposes of determining the constants, we have assumed a constant t_{ref} value in equation (2.1) for each partition in each dataset, corresponding to the appropriate plateau center. Assuming negligible difference in shift between in-gap and standalone, our process yields the following formula for the transferred

[2]For example, both use different trigger setups.

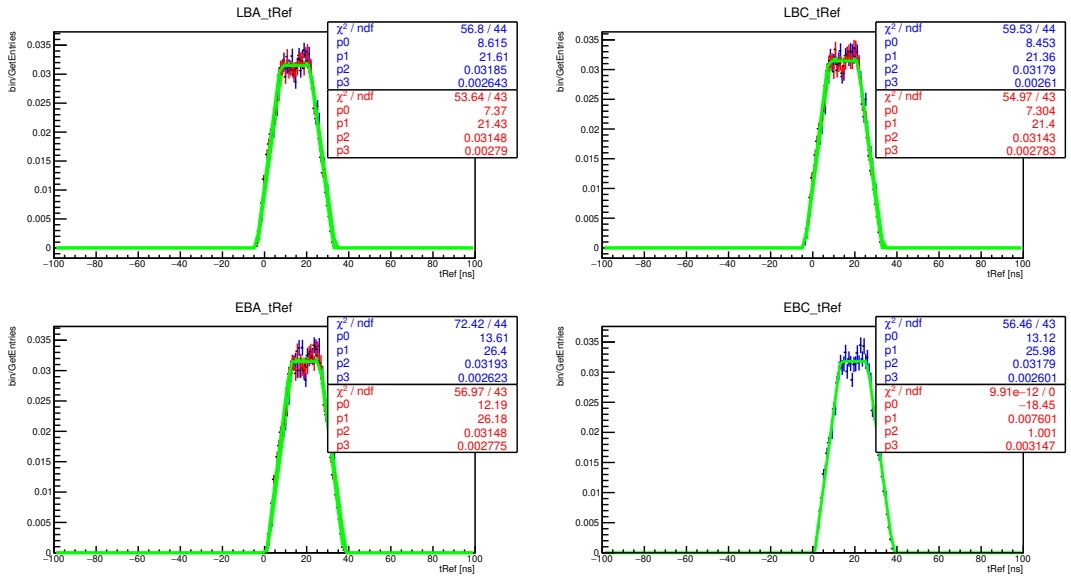

Figure 2.3: Four example histograms containing the t_{ref} values per partition in the standalone runs with trapezoidal fits. The red histogram represents data from 2018, the blue histogram contains values from 2021. The points of the fit correspond in order to: left end of the plateau, right end of the plateau, the left slope and the plateau height. EBC data from 2021 is missing due to the partition having been turned off in this particular run.

constants:

$$t_{\text{const}}(2021) = t_{\text{const}}(2018) + \langle t_{\text{reco}}(2021)\rangle - \langle t_{\text{reco}}(2018)\rangle. \tag{2.2}$$

2.2 Splash Events Calibration

2.2.1 Analysis of October 2021 Runs

Following the transfer of 2018 constants into the 2021 setup, four splash runs from October 2021 were analysed to determine the goodness of the constants used. The main advantage of the splash events is their comparatively high energy. Since the standard time resolution error at these energies is roughly 0.5 ns we can expect a high degree of precision despite the relatively smaller statistical volumes available.

We have used a slightly modified version of the laser calibration macro to analyse all four runs taken without time constants in October 2021. Extra attention was given to runs 404400 (mainly for macro debugging) and 405495 (latest run available). Similarly to the laser ntuple analysis, we have omitted data from problematic channels. Unlike in laser calibration, where the biggest issue was low goodness of fit caused by electronics, here we primarily had to cut channels subject to ADC saturation. We had also introduced further cuts for Low Gain events, signal peak position in regards to readout window center, and cell type.[3] For a channel to be viable for further statistical operations (analysis of mean value and RMS), we only considered histograms with at least five entries.[4]

[3] E cells were excluded due to consistent saturation issues and poor data quality.

[4] The 405495 run contains 19 entries total, with 18 primarily containing Low Gain data.

For better clarity, we had worked with average values across all modules. The comparatively low RMS for each channel (consistently valued under 1 ns) allowed us to analyse module-to-module differences while retaining information about general channel behaviour. To compare our constants to the well-calibrated state of TileCal in 2015, we attempted to reproduce the graphs in Fig. 1.5 (Figures 2.4, 2.5).

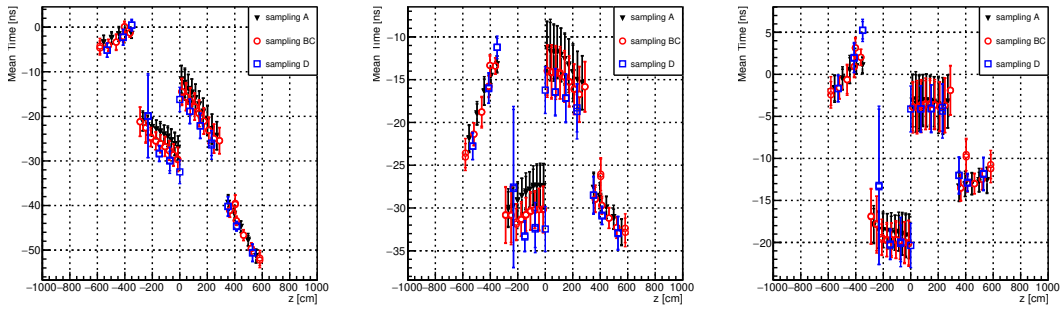

Figure 2.4: ϕ-average reconstructed times in run 405495 beam 1 (entry from A-side). Each line segment corresponds to data from one partition (from left to right: EBC, LBC, LBA, EBA). Each point represents the mean value across all modules. Error bars are defined as the RMS of the over-ϕ gaussian and remain constant in all three graphs.

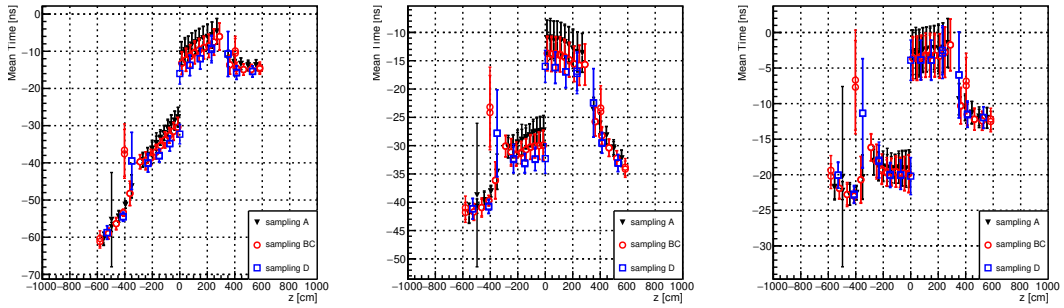

Figure 2.5: ϕ-average reconstructed times in beam 2 of the same run. In all four partitions, the shape of the distribution is worse than in beam 1, and the average RMS is also higher.

In the initial stages of the splash data analysis, we have omitted the T_0 term in equation (1.7). It was more important to determine deviations from the flat distribution in each partition, than to have all four partitions uniformly aligned near zero. The leftmost graphs in Figures 2.4, 2.5 show reconstructed times from the run ntuple using the transferred laser constants following the formula (2.1) with $t_{\text{ref}} \equiv 0$. The middle graphs show the application of the particle TOF correction following the

$$\langle t_{\text{reco}} \rangle = \langle t_{\text{splash}} \rangle - t_{\text{const}} + \frac{z_{\text{cell}}}{c} \tag{2.3}$$

The entry cut corresponds to roughly 28% of available data, which we considered a healthy benchmark for our desired degree of precision.

formula. The graphs on the right show values that follow the

$$\langle t_{\text{reco}} \rangle = \langle t_{\text{splash}} \rangle - t_{\text{const}} + \frac{z_{\text{cell}}}{c} + \frac{\sqrt{x^2 + y^2 + z^2}}{c} \tag{2.4}$$

formula, which is just a rearrangement of the modified equation (1.7).

Several issues had been immediately identified: in the extended barrel, there were significant deviations from a flat distribution along the length of the partition, and multiple channels were suffering from an excessively high RMS when averaged across all 64 modules. In beam 2, similar issues were encountered on an even larger scale, with several channels exhibiting asymmetrical behaviour in regards to beam direction. After a preliminary analysis, we had decided to focus on the beam 1 data in the long barrel, due to its better consistency with expected behavior and response to the corrections made.

After presenting our findings to the appropriate TileCal group, we had started work on identifying and eliminating the issues. One possible cause of problems we have considered were retriggered events. These occur when a fraction of the collimated bunch makes one additional orbit and triggers a separate splash event. Reconstructed times from these events are often shifted, and worsen the overall statistic, making them undesirable. However, every retriggered event can be easily identified by its comparatively lower energy deposit in the detector (see Fig. 2.6 for details specific to run 405495 beam 1).

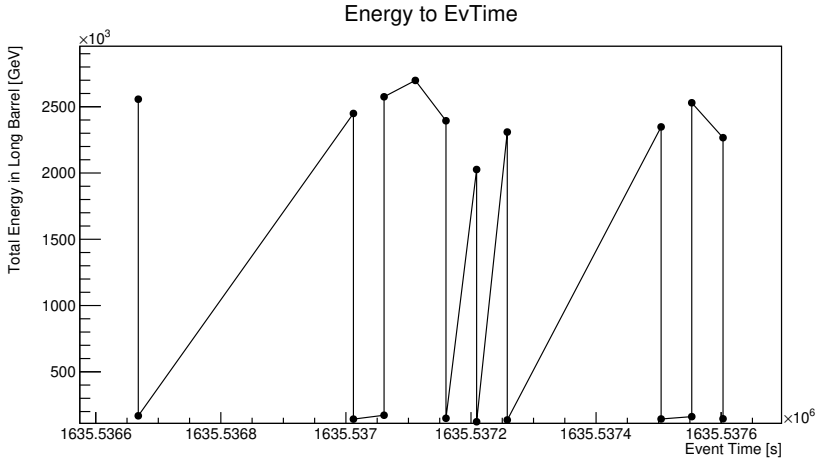

Figure 2.6: Graph of energy deposited in Long Barrel over event time. The events that occur quickly after the previous and yield a low energy deposit are very likely to be retriggered.

By introducing a cut at the 1 TeV mark for energy deposit in long barrel, we have been able to cut nine events with high probability of being retriggered. This led to negligible improvements in RMS for most channels as well as larger improvements in the RMS of the reconstructed channel time averages over ϕ, which will be discussed below. However, the overall shape of the distributions had not visibly improved after the cut; this suggested another, more intrinsic problem with our data.

We have observed a considerable difference between the RMS of individual channel histograms for each partition ($<$1 ns), and the RMS of the module-averaged histograms ($\approx$4 ns); this means that while the reconstructed times in

each channel are consistent with each other, the values for the same channel vary module to module. We have constructed a plot of all reconstructed time means per module for each LB partition to further analyze the reconstructed times (see Figures 2.7, 2.8).

In the LBA partition, several modules were identified as problematic; the values in modules in the LBA60-LBA04 range deviate from the rest by several ns in all channels; a separate analysis revealed no obvious cause of these problems. The LBA18 module was extremely oversaturated to the point of nearly half the channel histograms being empty; the few channels that could yield sufficient statistic volume were usually considerably shifted in time. The LBA37 module was found dead in every splash run, meaning its reconstructed time was set to zero by definition in every event. These two modules were taken out of the analysis entirely.

In LBC, no large shift corresponding to LBA60–LBA04 azimuthal area was observed. The LBC18 module suffered from similar problems to its LBA counterpart; high saturation and poor OF fit quality made it impossible to gather a decent-enough statistic for time calibration purposes. LBC63 visibly deviates in all values, with the shift increasing with proximity to barrel centre, but no explanation was found as to why. These two modules were also removed from further analysis.

A separate statistic was also made to track the RMS values in the histograms of over-ϕ averages. Before the retriggered events cut, the LBA partition had an average RMS of roughly 4.8 ns for each over-ϕ histogram, while the LBC partition had a corresponding value of 2.2 ns (see Fig. 2.9). After sanitizing the retriggered events and removing the four most problematic modules, those values had decreased to 3.3 ns and 1.6 ns respectively (Fig. 2.10).

When examining the LBA60–04 and LBA05–59 module ranges separately, we found that the LBA05–59 module range yields an average over-ϕ histogram RMS of roughly 1.3 ns (see Fig. 2.11). In comparison, the LBA60–04 histograms have an average RMS of about 2.2 ns. This suggests that the values in the LBA60-04 fluctuate more than those in the LBA05–59 range, hinting at a lack of self-consistency instead of an uniform shift. However, we were unable to find a sufficiently good explanation as to the strange behaviour of these modules.

Ultimately, the decision has been made to abandon the transferred constants from laser in favour of using the splash data to calibrate the constants. Despite the validity of the initial thought process behind the transfer of the constants, as well as the high degree of correlation between two types of laser calibration outlined in Fig. 2.2, it is clear that the constants used are not fit for calibration of TileCal at this time. Instead, we have used constants computed from the splash data itself using the formula given by (1.7) where possible.

For this purpose, we followed the conventions established in subsection 1.4.2 in addition to the cuts outlined previously in this subsection. The final statistic is roughly 6200 calibrated channels out of about 9700 non-empty channels in TileCal, with the main problem being event-by-event channel saturation and the following reduction in statistical volume below the set threshold. Our new constants were calculated using the formula (1.7).

A closure check had been performed to ensure the validity of our new constants, the results of which can be seen in Fig. 2.12.

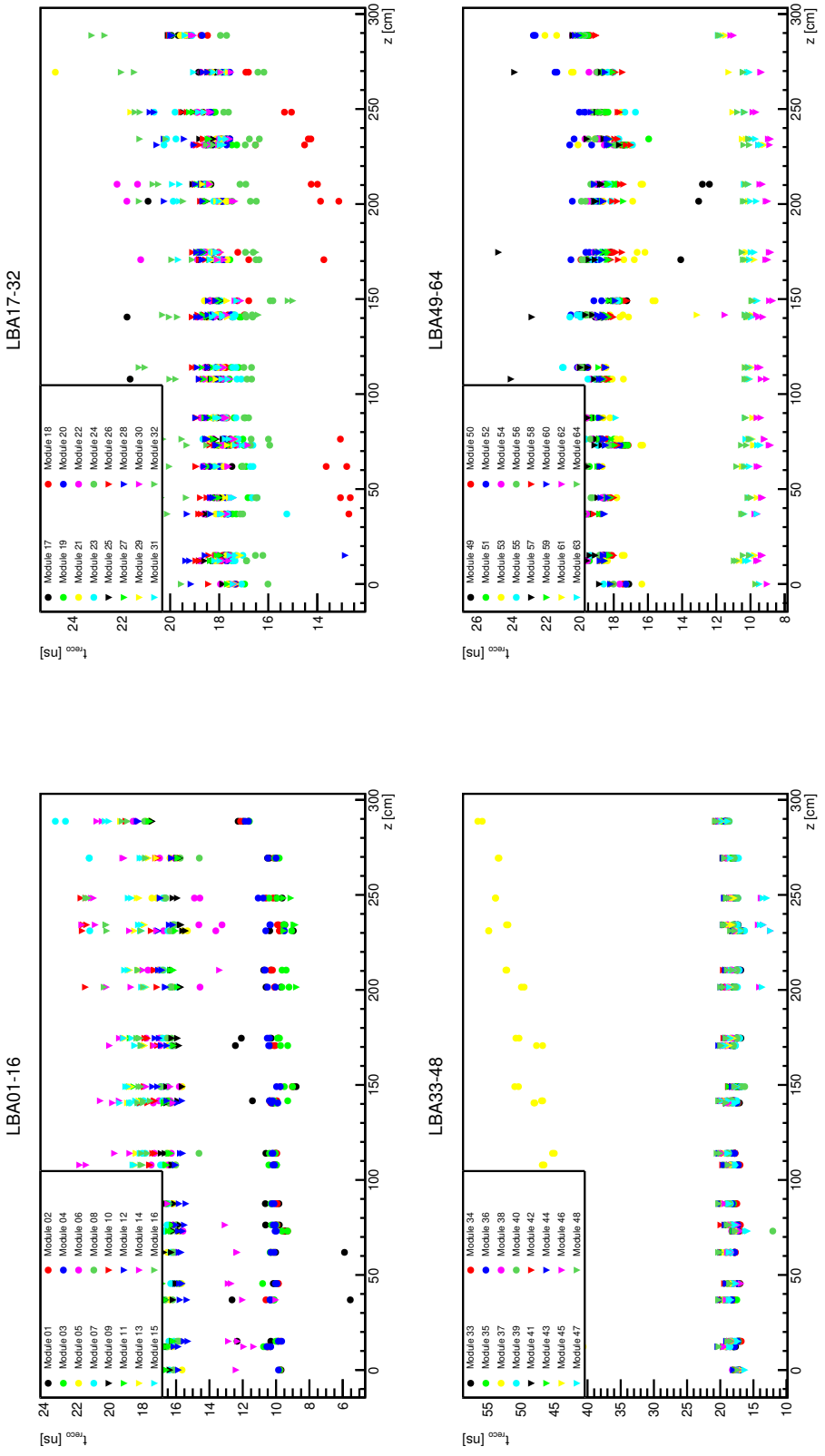

Figure 2.7: Graphs of reconstructed time means per module for LBA. Each graph contains values from 16 modules. The x-axis value represents the z-coordinate of each corresponding cell centre.

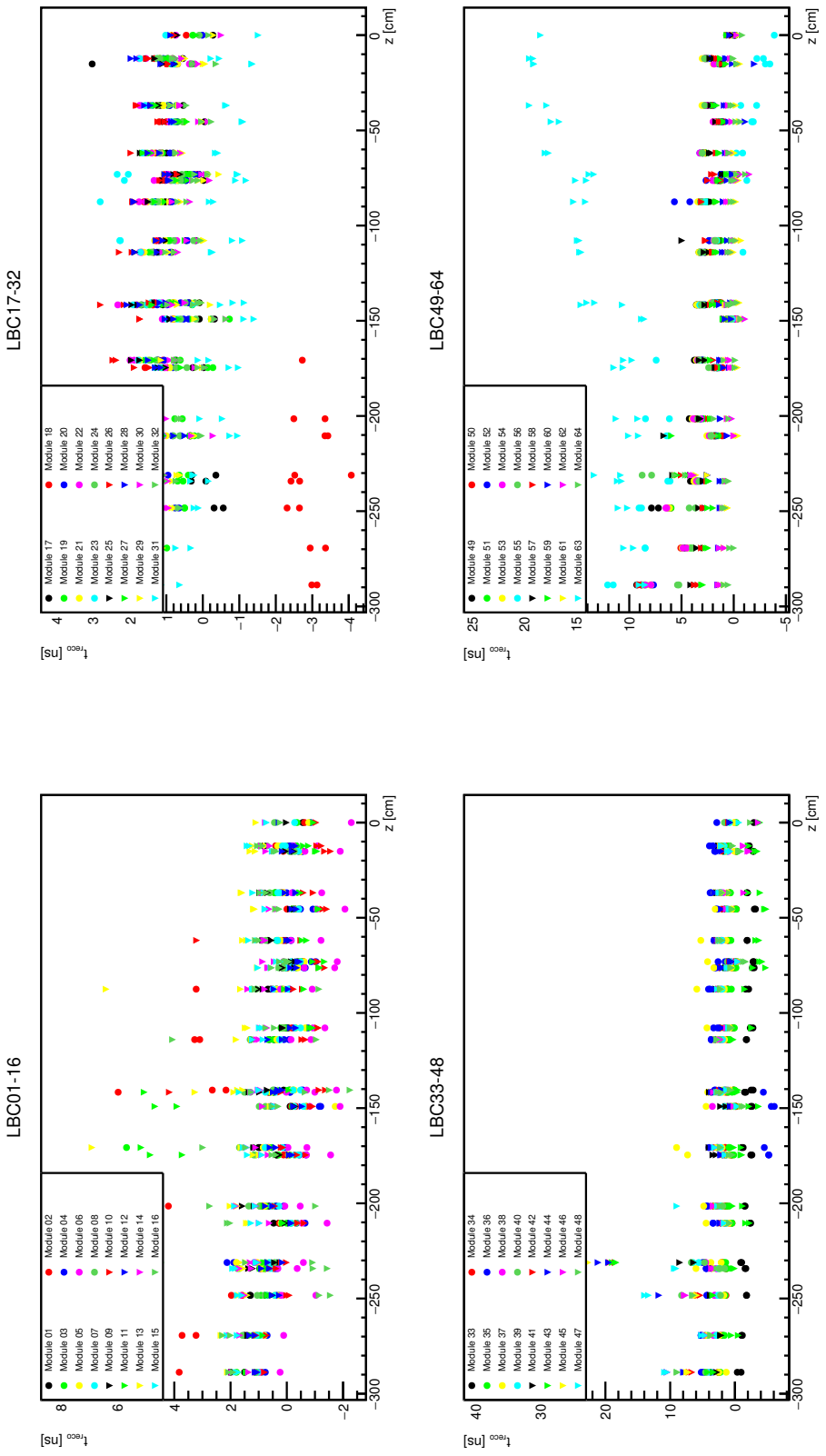

Figure 2.8: Graphs of reconstructed time means per module for LBC, following the same conventions as Fig. 2.7.

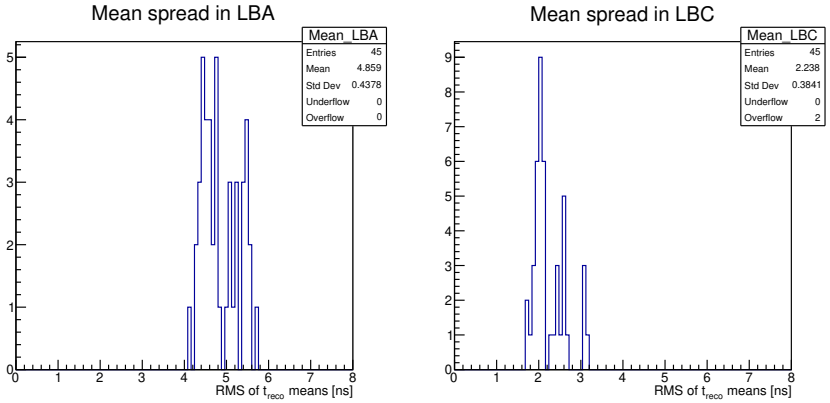

Figure 2.9: Histograms of RMS for each over-ϕ peak. These values correspond to initial analysis, before the retriggered events cut and the removal of LBA18, LBA37, LBC18, and LBC63 from the statistic.

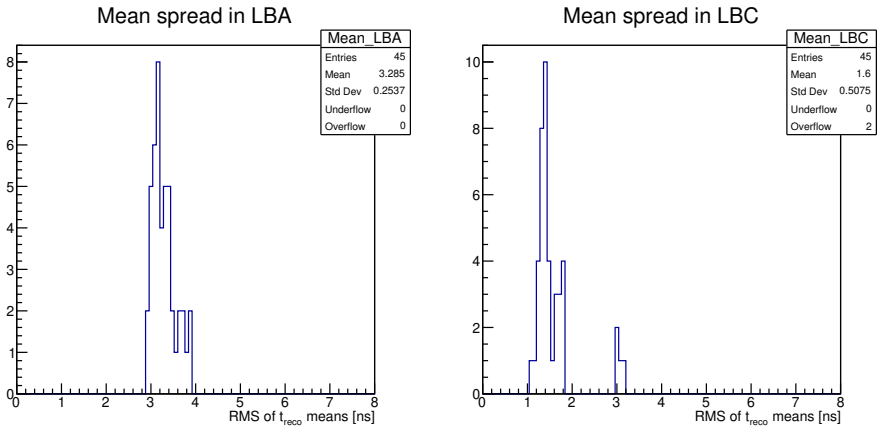

Figure 2.10: Histograms of RMS for each over-ϕ peak, after the retriggered event cut and the discrimination of problematic modules. A sharp decrease of mean RMS can be observed in both partitions.

One thing of note: although we've previously said that we expect a flat distribution near zero, we can now observe an offset of roughly 8.3 ns. We can deduce the reason behind this by further examination of the $t_{\text{splash}} - T_0$ term in equation (1.7). Since

$$T_0 = \frac{1}{N} \sum^{N} t_{\text{splash}}, \tag{2.5}$$

where the sum is done over N viable cell channels in the barrel centre, the introduction of constants (equal to a transformation of $t'_{\text{splash}} = t_{\text{splash}} - t_{\text{const}}$) yields

$$T'_0 = \frac{1}{N} \sum^{N} t'_{\text{splash}} = \frac{1}{N} \sum^{N} \left(t_{\text{splash}} - t_{\text{const}} \right). \tag{2.6}$$

Since the new t_{const} values were set from an ntuple that doesn't use any predetermined constants in its t_{splash} values, and the new ntuple does, a set of constants perfectly calibrated in regards to equation (1.7) creates a constant residual offset after the transformation described above. Combining equations (1.7), (2.4), (2.5)

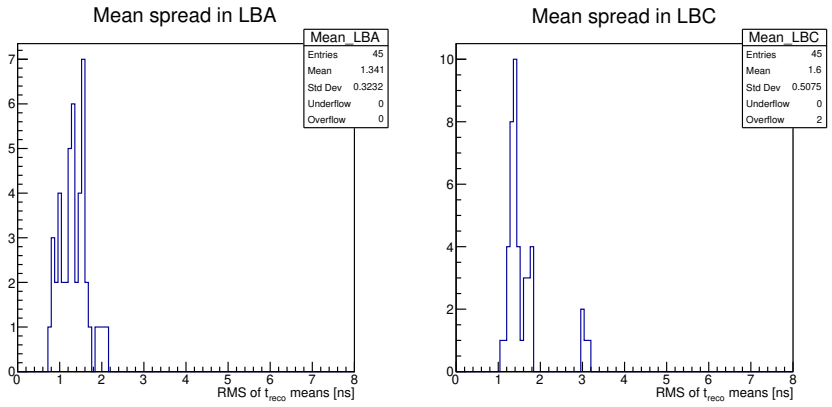

Figure 2.11: Histograms of RMS for each over-ϕ peak for the LBA05–59, LBC01–64 ranges, after cuts. The LBA histogram has been sanitized of most visibly problematic modules. The right histogram remains the same as in Fig. 2.10 by definition.

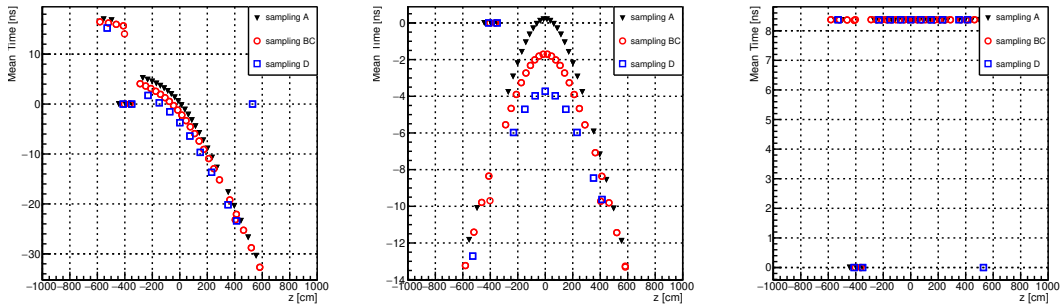

Figure 2.12: Three graphs following the same formula as Figures 2.4 and 2.5. It is clear that the combination of T_0 re-introduction and use of new constants yields a perfectly flat distribution. The points with no offset from zero correspond to channels that couldn't be calibrated in any of the 64 modules.

and (2.6) makes it obvious that

$$\begin{aligned} 0 \equiv &\langle t_{\text{reco}} \rangle = \langle t_{\text{splash}} - t_{\text{const}} - T_0 \rangle + \frac{z_{\text{cell}}}{c} + \frac{\sqrt{x^2+y^2+z^2}}{c} \\ \neq &\langle t'_{\text{reco}} \rangle = \langle t'_{\text{splash}} - T'_0 \rangle + \ldots = + \frac{1}{N} \sum^{N} t_{\text{const}}, \end{aligned} \tag{2.7}$$

where the right side is in our case equal to the 8.3 ns found in the offset in Fig. 2.12. This offset only disappears for $\frac{1}{N}\sum^{N} t_{\text{const}} = 0$; something which could be implemented via hardware adjustments.

Conclusion

We have performed a preliminary time calibration of the TileCal detector for the ATLAS experiment following the 2019–2022 maintenance period before Run 3. After initial analysis of the laser calibration from 2018, we have devised a method to transfer the constants from well-calibrated detector setup of Run 2 into the present time. Due to lack of laser-in-gap data from summer of 2021, we have improvised a workaround using values from standalone runs. The high degree of correlation in relative changes for both types of laser calibration between the properly calibrated setup in November 2018 and the last available data in June 2021 encouraged to follow through with our initial hypothesis. After scrutinizing the data and accounting for global reference time differences, we have transferred the constants from all healthy channels and utilized them in the initial splash analysis.

The results of the splash events pre-calibration yielded little success, but a great deal of information. The constants used did not properly reflect the expected behaviour of the splash times, bidding further analysis of new problems. Chief of these was the poor shape of the actual distribution with regard to expected behaviour. Several corrections were attempted, including elimination of likely retriggered events and removal of the most problematic modules from the statistic, but they were not enough to fix the underlying issues in the transferred constants setup. The results of our work were discussed at two meetings of the Tile Calorimeter group.

Ultimately, we deem the original aim of this thesis at least partially achieved. The time calibration of the detector is, as of spring 2022, an ongoing process. Although we were unable to convert our well-founded and well-supported hypothesis regarding the transfer of laser constants into tangible success, the extensive and ongoing modifications to the calorimeter provide a valid excuse as to why. The results of the splash event analysis were thus used to derive the new time calibration constants. About two thirds of all channels were calibrated, and we expect to continue our work on the rest once new splash data is acquired by end-of-April 2022.

Bibliography

[1] The ATLAS Collaboration. The ATLAS experiment at the CERN large hadron collider. *Journal of Instrumentation*, 3(08):S08003–S08003, Aug 2008.

[2] Tomáš Davídek. Instrumentace a kalibrace hadronového kalorimetru ATLAS TileCal. `https://www-ucjf.troja.mff.cuni.cz/~davidek/habilitace_text.pdf`. Habilitation thesis, Charles University, Prague, May 2013.

[3] A. Aad et al. Readiness of the ATLAS Tile Calorimeter for LHC collisions. *The European Physical Journal C*, Jan 2010.

[4] Tilecal Calibration, Data Quality, Performance and Processing. `http://atlas.web.cern.ch/Atlas/SUB_DETECTORS/TILE/`.

[5] J. Poveda J. Valls and A. Ferrer. Detector developments for the LHC: CMS TOB Silicon Detector Modules and ATLAS TileCal Read-Out Driver. Jan 2005.

[6] M. Aaboud et al. Operation and performance of the ATLAS Tile Calorimeter in Run 1. *The European Physical Journal C*, 78, Dec 2018.

[7] T. Davídek et al. Time calibration and monitoring in the Tile Calorimeter. Jun 2020.